

Burgers rings as topological signatures of Eshelby-like plastic events in glasses

Arabinda Bera¹, Ido Regev², Alessio Zaccone^{1,*} and Matteo Baggioli^{3†}

¹*Department of Physics “A. Pontremoli”, University of Milan, via Celoria 16, 20133 Milan, Italy*

²*Department of Solar Energy and Environmental Physics, Jacob Blaustein Institutes for Desert Research, Ben-Gurion University of the Negev, Sede Boqer Campus 84990, Israel and*

³*Wilczek Quantum Center & School of Physics and Astronomy, Shanghai Jiao Tong University, Shanghai 200240, China*

Eshelby-like quadrupolar structures serve as the fundamental microscopic units for characterizing plastic instabilities in amorphous solids and play a crucial role in explaining their mechanical failure, including the formation of shear bands. However, identifying Eshelby-like plastic events in glasses remains challenging due to their inherent structural and dynamical complexity. In this work, we show that Eshelby-like structures can be precisely identified and localized using a topological invariant known as the continuous Burgers vector. By combining analytical and simulation techniques, we reveal the emergence of a topological Burgers ring around Eshelby plastic events, enabling the precise identification of their center of mass and capturing their orientation as well. This proposed method offers a clear and unambiguous framework to locate and characterize the plastic rearrangements that govern plasticity in glasses.

Introduction – The description and quantification of plasticity and mechanical failure in crystalline materials [1] are based on the concept of structural defects [2], particularly topological defects (TDs), such as dislocations. A typical example is the Peierls-Nabarro theory of yield stress [3, 4]. In contrast, the elementary processes of plastic deformation in amorphous solids remain an open question [5–7], with significant implications for their practical applications.

This challenge primarily stems from the absence of an underlying lattice structure, which in crystals provides a well-defined “background” reference for identifying discrete defects. However, it was recognized early on that, in amorphous solids, structural relaxation tends to occur in localized regions exhibiting large non-affine displacements [8] and local stress drops [9]. These atomic rearrangements can be associated with quadrupolar zones and effectively described using the Eshelby inclusion model [10, 11]. It should be stressed that the Eshelby theory describes the stress and strain fields around, and inside, a heterogeneous inclusion (a spherical or ellipsoidal particle or void inside an otherwise homogeneous elastic medium), whereas, strictly, there are no such “inclusions” in the amorphous solids of interest here.

These Eshelby-like plastic events have been incorporated into several mesoscopic models of plasticity in glasses, grounded in the successful yet phenomenological concept of shear transformation zones (STZs) [5]. Moreover, the dynamics and, in particular, the alignment of these events have been identified as key factors in the formation of shear bands [12, 13], ultimately leading to plastic failure. Up to now, Eshelby-like quadrupolar defects and STZs remain the most widely used theoretical frameworks for characterizing and predicting plasticity in glasses, and are widely applied across a broad range of materials (e.g., [14, 15]).

Importantly, the stress drop induced by relaxation can

be effectively characterized by the location and orientation of fictitious Eshelby inclusions [14, 16]. Nevertheless, beyond idealized and simplified scenarios, identifying the precise location and orientation of these Eshelby-like plastic events remains highly non-trivial.

As comprehensively reviewed in [17], well-defined topological defects, particularly dislocation-type defects, can also be defined in disordered condensed matter systems, including amorphous solids. In these systems, dislocation-like TDs are still characterized by a continuous topological invariant: the Burgers vector. However, unlike in crystals, this vector is continuous-valued, and no longer “quantized” in units of the lattice spacing.

Building on these concepts, it was recently shown [18, 19] that the continuous Burgers vector, computed from the non-affine displacement field, serves as a useful indicator of plasticity in glasses, accurately predicting the location of the yielding instability. Recent work [20] further suggests that this topological invariant provides a robust and measurable metric for characterizing local structural transformations associated with plastic events.

More broadly, these developments are part of a growing research program that reintroduces the concepts of topology and topological defects to describe and rationalize plasticity in amorphous solids [18, 20–30]. Notably, Ref. [29] demonstrated that antivortex defects in the displacement field are strongly reminiscent of Eshelby inclusions in two-dimensional disordered solids, suggesting a possible method for identifying STZs. Additionally, topological defects have been used to reinterpret shear banding in metallic glasses [25] and to rationalize their formation through the emergence and dynamics of vortices [31].

In this work, we advance the idea that topological concepts play a crucial role in disordered systems such as glasses. Specifically, we show that the continuous Burgers vector can be effectively employed to identify Eshelby-like plastic events in two-dimensional sys-

tems. By combining analytical insights with simulation data, we demonstrate the emergence of Burgers “rings” encircling quadrupolar Eshelby-like structures (plastic events). Furthermore, these rings allow one to quantitatively determine the center of the Eshelby-type plastic event, something that could not be achieved thus far with

traditional Eshelby or STZ-type analyses.

Ideal Eshelby inclusion and Burgers ring – We start by considering the idealized Eshelby inclusion problem [10, 11]. The analytical solution for the elastic displacement field $\vec{u} \equiv (u_x, u_y)$ of a 2D Eshelby inclusion is given by (see [32] for a derivation):

$$\begin{aligned} u_x^{out}(r > a) &= \frac{\varepsilon^*}{4(1-\nu)} \frac{a^2}{r^2} \left\{ \left[2(1-2\nu) + \frac{a^2}{r^2} \right] [x \cos 2\phi + y \sin 2\phi] + \left[1 - \frac{a^2}{r^2} \right] \left[\frac{(x^2 - y^2) \cos 2\phi + 2xy \sin 2\phi}{r^2} \right] 2x \right\}, \\ u_y^{out}(r > a) &= \frac{\varepsilon^*}{4(1-\nu)} \frac{a^2}{r^2} \left\{ \left[2(1-2\nu) + \frac{a^2}{r^2} \right] [x \sin 2\phi - y \cos 2\phi] + \left[1 - \frac{a^2}{r^2} \right] \left[\frac{(x^2 - y^2) \cos 2\phi + 2xy \sin 2\phi}{r^2} \right] 2y \right\}, \end{aligned} \quad (1)$$

and:

$$\begin{aligned} u_x^{in}(r < a) &= \frac{\varepsilon^*}{4(1-\nu)} (3-4\nu) [x \cos 2\phi + y \sin 2\phi], \\ u_y^{in}(r < a) &= \frac{\varepsilon^*}{4(1-\nu)} (3-4\nu) [x \sin 2\phi - y \cos 2\phi], \end{aligned} \quad (2)$$

where *out-in* correspond respectively to the region outside ($r > a$) and inside ($r < a$) the inclusion, with $r \equiv \sqrt{x^2 + y^2}$. We notice that the displacement field is continuous at $r = a$ but its derivatives with respect to x, y are not. Here, ε^* is the eigenstrain magnitude, ν is the Poisson ratio, and a is the radius of the inclusion. The parameter ϕ represents the orientation of the quadrupolar zone, while r denotes the radial distance from the quadrupole’s center. The coordinates (x, y) specify a point relative to the quadrupole’s center, which is taken for simplicity as the origin $(0, 0)$. The displacement field of an ideal Eshelby inclusion, corresponding to the expressions in Eqs. (1)-(2), is shown in Fig. 1(a). The displacement field is illustrated for an Eshelby inclusion centered at $(0.5, 0.5)$ with a radius $a = 0.05$. The other parameters are set to $\varepsilon^* = 1$, $\nu = 0.46$ and $\phi = \pi/4$. The characteristic quadrupolar symmetry is evident.

Leveraging on the analytical expression, Eq. (1) and Eq. (2), we compute the Burgers vector \vec{b} [18, 33],

$$b_i = - \oint_{\mathcal{L}} du_i = - \oint_{\mathcal{L}} \frac{du_i}{dx^k} dx^k, \quad (3)$$

with \mathcal{L} a closed loop of arbitrary shape, that for simplicity is taken to be a circle of radius $R = a/2$ centered at (x_0, y_0) (see Supplementary Material, SM). The Burgers vector is then evaluated by systematically varying the loop center (x_0, y_0) over the two-dimensional grid. The Burgers vector magnitude for this ideal case is shown in Fig. 1(b). The value of the Burgers vector is nonzero only along a localized ring, from now on labeled as the *Burgers ring*, that coincides with the core $r = a$ of the (fictitious) inclusion. The Burgers ring arises due to the

discontinuity of the strain tensor at the inclusion boundary $r = a$. Consequently, any loop integral defined as in Eq. (3), where the integration path \mathcal{L} intersects the circle $r = a$, yields a finite value of \vec{b} .

Interestingly, the amplitude of \vec{b} along the Burgers ring captures the orientation of the Eshelby inclusion, as demonstrated in Fig. 1(c). Indeed, the amplitude of the Burgers vector along the ideal Burgers ring, $r = a$, shows a periodic pattern with minima at azimuthal angle $\theta = \pi/4, 3\pi/4, 5\pi/4, 7\pi/4$. The first minimum of $|\vec{b}|$ aligns with the principal axis of the Eshelby inclusion in Fig. 1(a), in this representative example.

Topological defects and plastic spots – In order to go beyond the ideal scenario discussed above, we simulate a two-dimensional glass model [34]. Detail of the system are provided in the Supplementary Material (SM). In Fig. 2(a) we show a particle displacement field generated by a plastic event (see Supplementary Material for further explanations). In this case, there is one Eshelby-like “soft-spot” [35], featuring approximate quadrupolar symmetry, which is marked with a green circle for better clarity.

We interpolate the displacement field onto a 32×32 lattice grid. In Fig. 2(b) we show the normalized displacement field $\hat{u} \equiv \vec{u}/|\vec{u}|$, mapped onto the same lattice grid, where the corresponding color indicates its amplitude $|\vec{u}|$. After normalizing the vector field, spatial structures (e.g., swirlings) appear. In order to describe the topology of the displacement field, we resort to the concept of winding number q . In two dimensions, the local winding number is given by:

$$q = \frac{1}{2\pi} \oint_{\mathcal{L}} d\theta, \quad (4)$$

where θ is the direction of \vec{u} . When \mathcal{L} is chosen as the smallest loop possible, then local regions with $q = \pm 1$ correspond respectively to the presence of a vortex/anti-vortex topological defect.

These vortex-like topological defects have been re-

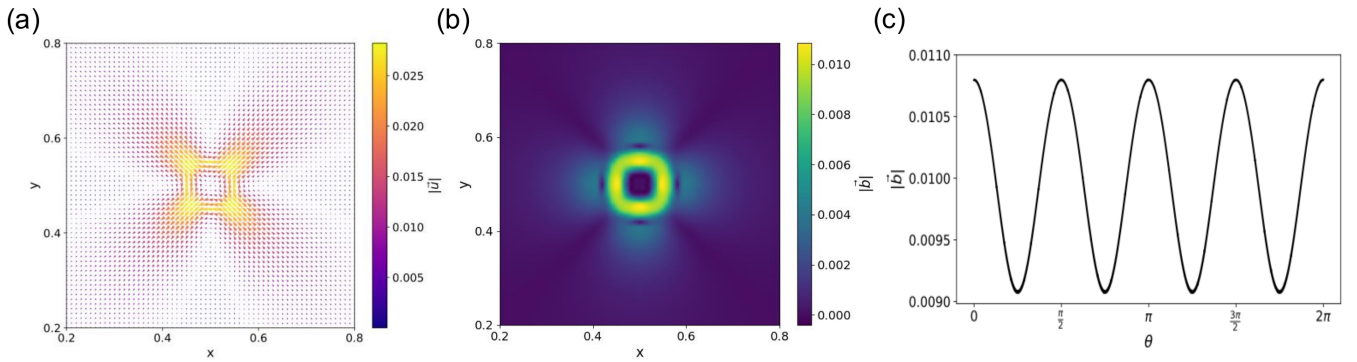


FIG. 1: **(a)** The displacement field for an ideal Eshelby inclusion centered at $(x, y) = (0.5, 0.5)$ is shown. The color bar indicates the magnitude of the displacement field. For this case we have fixed $\varepsilon^* = 1$, $\nu = 0.46$, $\phi = \pi/4$ and $a = 0.05$. **(b)** The magnitude of the Burgers vector is shown with a color bar. The circular ring around $r = a$ is prominent. **(c)** The variation of $|\vec{b}|$ along the azimuthal angle θ along the Burgers ring $r = a$.

cently related to the characteristics of Eshelby inclusions [29]. However, as we will explicitly demonstrate, the concept of vortex-like topological defects alone is insufficient to accurately identify quadrupolar Eshelby-like plastic events in two-dimensional amorphous systems.

Red and blue circles in Fig. 2(b) identify respectively vortices ($q = +1$) and anti-vortices ($q = -1$). Consistent with the analysis of [29], we find that an anti-vortex emerges at the core of the Eshelby-like structure. Nevertheless, it is not the only one: we observe other topological defects with a rather ordered spatial correlation. We notice that the total winding number within the simulation box remains zero due to the application of periodic boundary conditions in both directions and the Poincaré-Hopf index theorem [36].

In order to properly identify the plastic spots, we further look for the relative particle displacement with respect to their neighbors and compute the standard metric D_{\min}^2 [8] (see details in SM). As shown in Fig. 3(a), the magnitude of D_{\min}^2 is highest around the Eshelby-like structure and confirms that not all topological antivortex-like defects in Fig. 2(b) are related to plastic spots.

Moreover, in Fig. 3(b) we show the amplitude of the quadrupolar charge Q (see for example [37]), defined by decomposing the symmetric strain tensor \mathbf{s} as

$$\mathbf{s} = m\mathbf{I} + \mathbf{Q}, \quad (5)$$

with \mathbf{I} being the two-dimensional identity matrix and \mathbf{Q} the quadrupole tensor. A few mathematical identities leads to the definition (for more details see the SM):

$$Q = \frac{1}{2} \sqrt{(s_{xx} - s_{yy})^2 + 4s_{xy}^2}, \quad (6)$$

with $s_{ij} = 1/2 (\partial_i u_j + \partial_j u_i)$.

As shown in Fig. 3(b), the Eshelby-like plastic event in Fig. 2(a) has a strong quadrupolar nature, corresponding

to a large value of Q . On the other hand, in the rest of the (x, y) plane, Q vanishes or it is at least negligibly small.

Several key conclusions can be drawn from the investigation of the simulation data. (I) The positions of (anti)vortex-like topological defects alone are insufficient to precisely identify the Eshelby-like structures associated with plastic events. (II) The distribution of D_{\min}^2 and Q offers only an approximate indication of the location of these events and does not allow for an accurate determination of their center of mass. (III) There is no evident correlation between the locations of (anti)vortex-like topological defects in the displacement field and either D_{\min}^2 or Q , casting doubt on the effectiveness of (anti)vortex-like defects as indicators of plasticity.

Burgers ring – We then compute the local value of the Burgers vector \vec{b} on the simulated 2D displacement field using a closed circular loop of radius $R = 0.12$, while varying the loop center (x_0, y_0) across the simulation box, similar to the ideal Eshelby case. The results corresponding to the case presented in Fig. 2(a) are shown in Fig. 4(a). We observe that, like the results in the idealized case in Fig. 1(b), the Burgers vector is generally zero everywhere apart from a thin shell that is located exactly around the Eshelby-like quadrupolar structure. This result suggests that, even in a more realistic scenario, Eshelby-like plastic events are surrounded by a Burgers ring. Nevertheless, within the precision of our numerical data we are not able to ascertain whether the distribution of the Burgers vector captures the orientation of the Eshelby-like structure as well, as previously demonstrated for the idealized case. Partially, this might be also caused by the fact that in the simulations the Eshelby-like events do not display perfect quadrupolar symmetry and therefore their orientation is not neatly defined.

Three additional cases are presented in Appendix A in the *End Matter*, confirming the universality of our find-

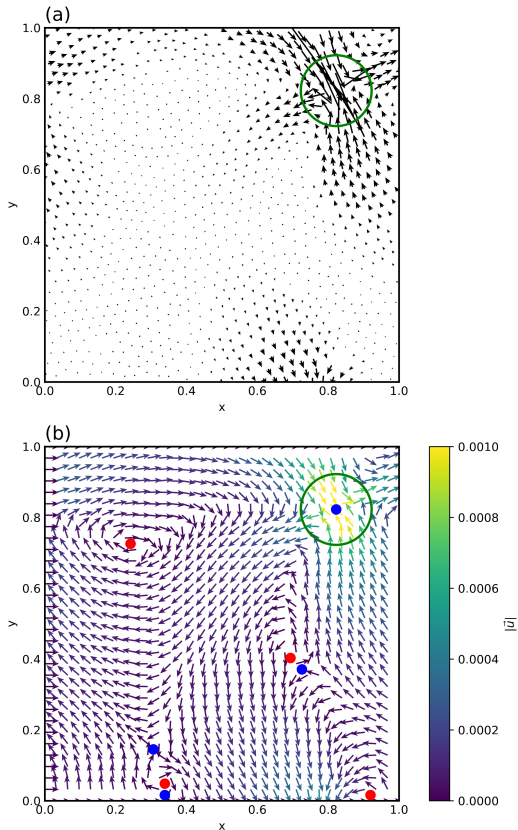


FIG. 2: (a) Particle displacement field. The circle highlights the region where an Eshelby-like structure emerges. (b) Normalized displacement vector field on a 32×32 lattice grid. Topological defects with winding numbers $+1$ and -1 are marked in red and blue, respectively. The color bar indicates the magnitude of the displacement field.

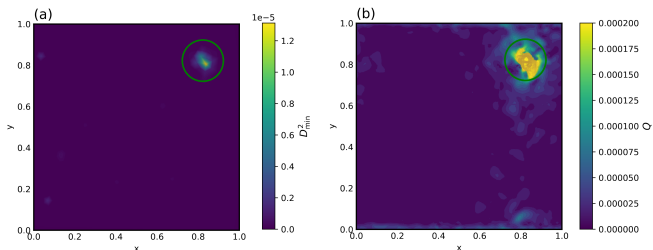


FIG. 3: (a) Spatial maps of the non-affine displacement measure D_{\min}^2 . (b) The magnitude of quadrupole charge Q at lattice grid is shown. The color bar represents the value of Q . The highlighted circle marks the region associated with an Eshelby-like rearrangement.

ings. Moreover, the stability of the results upon changing the loop radius R is demonstrated in the SM.

To further demonstrate the ability of the Burgers ring to locate the plastic events, in Fig. 4(b) we present a zoomed-in view where the top 1% of highest values of $|\vec{b}|$ around the plastic event are marked with black crosses. As also evident from this representation, a circular ring

is formed around the Eshelby-like structure. We then compute the center of mass of these points, that is indicated with a red open circle. We find that the center of mass, identified using the Burgers ring method, is very close to the -1 topological defect lying at the center of the quadrupolar Eshelby-like structure, and already presented in Fig. 2(b).

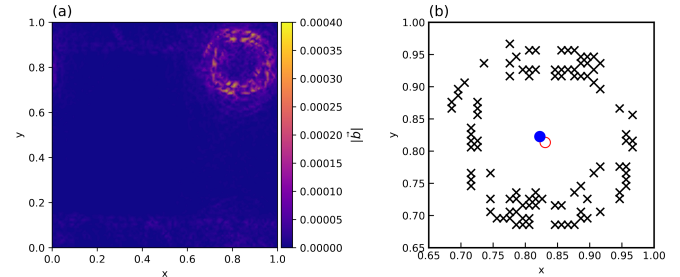


FIG. 4: (a) The magnitude of the Burgers vector is shown. (b) The locations having highest value of $|\vec{b}|$ are represented by black crosses. Their resulting center of mass is indicated with an open red circle. The location of the -1 TD is indicated by a blue filled circle.

Conclusions – In this work, we have shown that the local value of the continuous Burgers vector \vec{b} can be effectively used to identify Eshelby-like quadrupolar plastic events in two-dimensional amorphous solids. Specifically, \vec{b} becomes nonzero only along a localized structure, a “Burgers ring”, that encircles the core of the Eshelby-like deformation.

Compared to other existing methods, such as (anti)vortex-like topological defects [22], the D_{\min}^2 metric [8], and the quadrupolar charge Q [37], the Burgers ring approach offers significant advantages. In particular, (anti)vortex-like topological defects fail to reliably identify the location of Eshelby-like events, as they also appear in regions unrelated to plastic deformation. Additionally, unlike D_{\min}^2 or the quadrupolar charge Q , our method enables precise identification of the center of mass of these quadrupolar plastic events, in good agreement with the location of the antivortex defect [29].

In summary, we provide a robust and well-defined topological metric to accurately identify and locate Eshelby-like plastic events in 2D glasses. In the future, it would be interesting to extend this program to experimental data, as already attempted in [20], and to three-dimensional systems, where other topological measures have been already applied [27, 28, 38].

Acknowledgments – AZ is indebted to Prof. Srikanth Sastry for stimulating discussions and for providing a motivation to carry out this research. MB acknowledges the support of the Shanghai Municipal Science and Technology Major Project (Grant No.2019SHZDZX01) and the support of the sponsorship from the Yangyang Development Fund. AZ gratefully acknowledges funding from the European Union through Horizon Europe ERC Grant

number: 101043968 “Multimech”. AB and AZ gratefully acknowledge funding from the US Army DEVCOM Army Research Office through Contract No. W911NF-22-2-0256. IR was supported by the Israel Science Foundation (grant No. 1204/23).

* alessio.zaccone@unimi.it

† b.matteo@sjtu.edu.cn

- [1] E. Schmid and W. Boas, *Plasticity of Crystals: With Special Reference to Metals* (Chapman & Hall, 1968).
- [2] A. Sutton, *Physics of Elasticity and Crystal Defects*, Oxford Series on Materials Modelling (OUP Oxford, 2020).
- [3] R. Peierls, *Proceedings of the Physical Society* **52**, 34 (1940).
- [4] F. R. N. Nabarro, *Proceedings of the Physical Society* **59**, 256 (1947).
- [5] M. L. Falk and J. Langer, *Annual Review of Condensed Matter Physics* **2**, 353 (2011).
- [6] A. Tanguy, *Comptes Rendus. Physique* **22**, 117 (2021).
- [7] L. Berthier, G. Biroli, L. Manning, and F. Zamponi, *Nature Reviews Physics* (2025), 10.1038/s42254-025-00833-5.
- [8] M. L. Falk and J. S. Langer, *Phys. Rev. E* **57**, 7192 (1998).
- [9] C. Fusco, T. Albaret, and A. Tanguy, *Phys. Rev. E* **82**, 066116 (2010).
- [10] J. D. Eshelby and R. E. Peierls, *Proceedings of the Royal Society of London. Series A. Mathematical and Physical Sciences* **241**, 376 (1957).
- [11] J. D. Eshelby and R. E. Peierls, *Proceedings of the Royal Society of London. Series A. Mathematical and Physical Sciences* **252**, 561 (1959).
- [12] R. Dasgupta, H. G. E. Hentschel, and I. Procaccia, *Phys. Rev. Lett.* **109**, 255502 (2012).
- [13] V. Hieronymus-Schmidt, H. Rösner, G. Wilde, and A. Zaccone, *Phys. Rev. B* **95**, 134111 (2017).
- [14] T. Albaret, A. Tanguy, F. Boioli, and D. Rodney, *Phys. Rev. E* **93**, 053002 (2016).
- [15] S. McNamara, J. Crassous, and A. Amon, *Phys. Rev. E* **94**, 022907 (2016).
- [16] A. Nicolas and J. Rottler, *Phys. Rev. E* **97**, 063002 (2018).
- [17] M. Kleman and J. Friedel, *Rev. Mod. Phys.* **80**, 61 (2008).
- [18] M. Baggioli, I. Kriuchevskiy, T. W. Sirk, and A. Zaccone, *Phys. Rev. Lett.* **127**, 015501 (2021).
- [19] M. Baggioli, M. Landry, and A. Zaccone, *Phys. Rev. E* **105**, 024602 (2022).
- [20] A. C. Y. Liu, H. Pham, A. Bera, T. C. Petersen, T. W. Sirk, S. T. Mudie, R. F. Tabor, J. Nunez-Iglesias, A. Zaccone, and M. Baggioli, “Measurable geometric indicators of local plasticity in glasses,” (2024), [arXiv:2410.09391 \[cond-mat.soft\]](https://arxiv.org/abs/2410.09391).
- [21] M. Baggioli, *Nature Communications* **14**, 2956 (2023).
- [22] Z. W. Wu, Y. Chen, W.-H. Wang, W. Kob, and L. Xu, *Nat. Commun* **14**, 2955 (2023).
- [23] A. Bera, M. Baggioli, T. C. Petersen, T. W. Sirk, A. C. Y. Liu, and A. Zaccone, *PNAS Nexus* **3**, pgae315 (2024).
- [24] V. Vaibhav, A. Bera, A. C. Y. Liu, M. Baggioli, P. Keim, and A. Zaccone, *Nature Communications* **16**, 55 (2025).
- [25] H. Rösner, A. Bera, and A. Zaccone, *Phys. Rev. B* **110**, 014107 (2024).
- [26] L.-Z. Huang, Y.-J. Wang, and M. Baggioli, “Spotting structural defects in crystals from the topology of vibrational modes,” (2024), [arXiv:2410.04720 \[cond-mat.mtrl-sci\]](https://arxiv.org/abs/2410.04720).
- [27] A. Bera, A. Zaccone, and M. Baggioli, “Hedgehog topological defects in 3d amorphous solids,” (2025), [arXiv:2407.20631 \[cond-mat.soft\]](https://arxiv.org/abs/2407.20631).
- [28] Z. W. Wu, J.-L. Barrat, and W. Kob, “On the geometry of topological defects in glasses,” (2024), [arXiv:2411.13853 \[cond-mat.dis-nn\]](https://arxiv.org/abs/2411.13853).
- [29] P. Desmarchelier, S. Fajardo, and M. L. Falk, *Phys. Rev. E* **109**, L053002 (2024).
- [30] Z. Zheng, C. Jiang, Y. Chen, M. Baggioli, and J. Zhang, “Topological signatures of collective dynamics and turbulent-like energy cascades in active granular matter,” (2025), [arXiv:2504.02588 \[cond-mat.soft\]](https://arxiv.org/abs/2504.02588).
- [31] D. Soppu, *Journal of Alloys and Compounds* **960**, 170585 (2023).
- [32] R. Dasgupta, H. G. E. Hentschel, and I. Procaccia, *Phys. Rev. E* **87**, 022810 (2013).
- [33] H. Kleinert, *Gauge Fields in Condensed Matter*, Gauge Fields in Condensed Matter No. v. 2 (World Scientific, Singapore and Teaneck, N.J., 1989).
- [34] I. Regev, T. Lookman, and C. Reichhardt, *Phys. Rev. E* **88**, 062401 (2013).
- [35] M. L. Manning and A. J. Liu, *Physical Review Letters* **107**, 108302 (2011).
- [36] M. P. Do Carmo, *Differential Geometry of Curves and Surfaces: Revised and Updated Second Edition* (Courier Dover Publications, 2016).
- [37] C. Mondal, M. Moshe, I. Procaccia, and S. Roy, *Phys. Rev. E* **108**, L042901 (2023).
- [38] Y. Cao, J. Li, B. Kou, C. Xia, Z. Li, R. Chen, H. Xie, T. Xiao, W. Kob, L. Hong, J. Zhang, and Y. Wang, *Nature Communications* **9**, 2911 (2018).
- [39] E. Lerner and I. Procaccia, *Physical Review E—Statistical, Nonlinear, and Soft Matter Physics* **79**, 066109 (2009).
- [40] M. P. Allen and D. J. Tildesley, *Computer Simulation of Liquids* (Oxford University Press, 2017).
- [41] E. Bitzek, P. Koskinen, F. Gähler, M. Moseler, and P. Gumbsch, *Physical Review Letters* **97**, 170201 (2006).
- [42] A. W. Lees and S. F. Edwards, *Journal of Physics C: Solid State Physics* **5**, 1921 (1972).

End Matter

Appendix A: Universality of our findings - In order to confirm the universality of our findings, we have studied the displacement field and its characteristics across various plastic events observed in the stress-strain curve. In Fig. 5, we present three representative cases. Panels (a-c) show the displacement vector field (black arrows) with a superimposed color map of the coarse-grained D_{\min}^2 . In all three cases, isolated Eshelby-like plastic spots are recognized and correspond to regions with large D_{\min}^2 . In the corresponding panels (d-f), we display the local value of the Burgers vector amplitude $|\vec{b}|$. The locations of topological defects with winding number -1 inside the

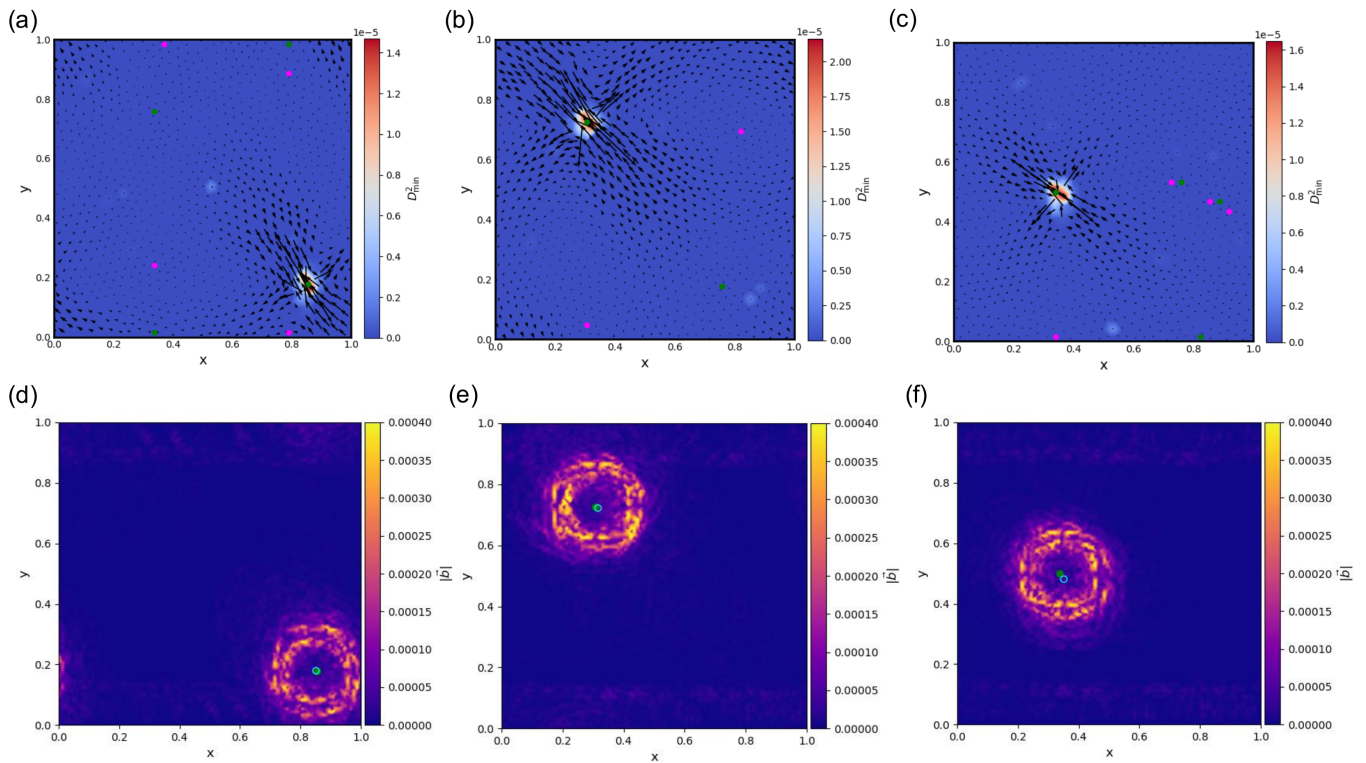


FIG. 5: **(a-c)** Several snapshots of the displacement vector field during plastic events. The background color map indicates the local value of D_{\min}^2 and helps identifying the quasi-localised Eshelby-like soft spots. The positions of topological defects with winding numbers $q = +1$ and -1 are indicated by magenta and green filled circles, respectively. **(d-f)** The corresponding map of the Burgers vector amplitude $|\vec{b}|$. The Burgers rings surrounding the Eshelby-like plastic events are evident. The white open circle is the center of mass of the Burgers ring, while the green disk is the location of the -1 anti-vortex topological defect located at the center of the Eshelby-like plastic spot.

Burgers rings and the center of mass of the top 1% highest $|\vec{b}|$ values are shown by green filled circles and an open circle, respectively. As evident, in all cases we observed

a very neat Burgers ring surrounding the Eshelby-like plastic events and confirming the findings presented in the main text.

Supplementary Material

Simulation details and stress-strain curve

We consider a two-dimensional system of point-like particles interacting via a radially-symmetric, attractive-repulsive, pairwise potential $U(r)$, where r denotes the distance between particle centers. The pair-wise potential consists of the repulsive part of the standard Lennard-Jones potential, connected via a hump to a region that is smoothed continuously to zero. Specifically, the interaction potential takes the form [34, 39]:

$$U(r) = \begin{cases} \varepsilon \left[\left(\frac{\sigma}{r}\right)^{12} - \left(\frac{\sigma}{r}\right)^6 + \frac{1}{4} - h_0 \right], & r \leq \sigma x_0, \\ \varepsilon h_0 P\left(\frac{r/\sigma - x_0}{x_c}\right), & \sigma x_0 < r \leq \sigma(x_0 + x_c), \\ 0, & r > \sigma(x_0 + x_c). \end{cases} \quad (\text{S1})$$

Here, ε sets the energy scale, and σ is the characteristic length scale of interaction. The potential minimum occurs at $x_0 = 2^{1/6}$, corresponding to the standard location of the minimum in the Lennard-Jones potential. Beyond this minimum, the potential is smoothly deformed using a polynomial $P(x)$, ensuring continuity up to the second derivative and allowing a gradual decay to zero at $r = \sigma(x_0 + x_c)$. The parameter h_0 controls the depth of the potential well. All of the variables and constants are given in Lennard-Jones units [34, 40].

The smoothing function $P(x)$ is a sixth-order polynomial defined as:

$$P(x) = \sum_{i=0}^6 A_i x^i, \quad (\text{S2})$$

with coefficients:

$$\begin{aligned} A_0 &= -1.0, & A_1 &= 0.0, & A_2 &= 1.785826183464224, \\ A_3 &= 28.757894970278530, & A_4 &= -81.988642011620980, \\ A_5 &= 76.560294378549440, & A_6 &= -24.115373520671220. \end{aligned}$$

The variation of $U(r)$ with r is shown in Fig. S1(a). Our simulation included a system of $N = 1024$ particles interacting via the potential $U(r)$ where for each pair of particles i and j the value of σ was chosen to be:

$$\sigma = \frac{\sigma_i + \sigma_j}{2},$$

where σ_i is the radius of particle i and σ_j is the radius of particle j . To prevent crystallization, we used a binary mixture where half the particles had a radius $\sigma_i = 1$ and the other half had a radius of $\sigma = 1.4$. The system was kept at a constant volume with a constant density of $\rho = 0.75$, in which the system is in a jammed state. In the figures shown in the text, the coordinates are normalized such that the simulation square has a side of size 1.

To prepare amorphous solids we first simulated a liquid at high temperature, using leap-frog integration combined with the Berendsen thermostat. We then cooled the liquid to a lower temperature and minimized the energy to zero using the FIRE minimization algorithm [41]. The protocol details are given in [34].

A representative snapshot of the resulting amorphous solid is shown in Fig. S1(b), where small black circles indicate particles of radius 1 and large red circles represent particles of size 1.4. We then applied shear using the athermal quasistatic (AQS) scheme where shear strain steps of magnitude 10^{-4} using the Lees-Edwards periodic boundary conditions [42] (black arrows in Fig. S1(b) indicate one of two possible shear directions). After each strain step, the energy was minimized using the FIRE algorithm in order to achieve a mechanically stable, zero temperature, configuration. When repeated many times, this scheme produces a typical stress-strain curve, as is shown in Fig. S1(c). In this curve, straight lines indicate elastic response, while stress drops indicate plastic events. The Eshelby structures discussed in the text are all results of such plastic transitions.

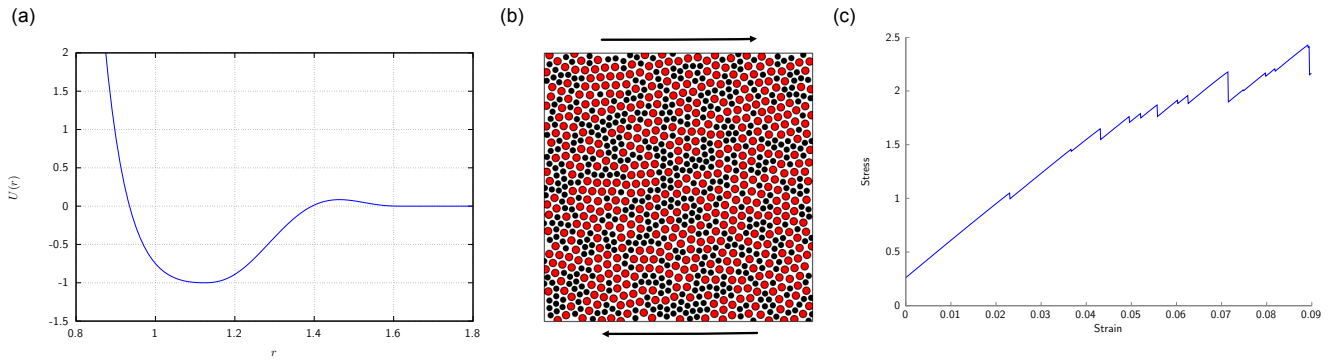


FIG. S1: **(a)** The interaction potential, Eq. S1 with $h_0 = 1$, $\epsilon = 1$, $\sigma = 1$ and $x_c = 0.5$. **(b)** A typical simulation box with arrows showing the directions of shear. **(c)** A typical stress-strain curve generated from the AQS simulation. We can observe that the increase in the stress as a function of strain is linear most of the time, but that once in a while there is a sharp drop in the stress, indicating a plastic event similar to the ones discussed in the text.

Computation of the Burgers vector

In a two-dimensional space parameterized by Cartesian coordinates (x, y) , the Burgers vector can be written as:

$$b_x = - \oint_{\mathcal{L}} \left(\frac{\partial u_x}{\partial x} dx + \frac{\partial u_x}{\partial y} dy \right), \quad b_y = - \oint_{\mathcal{L}} \left(\frac{\partial u_y}{\partial x} dx + \frac{\partial u_y}{\partial y} dy \right), \quad (\text{S3})$$

with \mathcal{L} being a closed loop of arbitrary shape.

For simplicity, we consider a circular loop of radius R centered at (x_0, y_0) , described in parametric form by $x = x_0 + R \cos(t)$ and $y = y_0 + R \sin(t)$, where the variable t varies from 0 to 2π . Substituting these expressions, we obtain:

$$b_x = \int_0^{2\pi} dt R \left(\frac{\partial u_x}{\partial x} \sin t - \frac{\partial u_x}{\partial y} \cos t \right), \quad b_y = \int_0^{2\pi} dt R \left(\frac{\partial u_y}{\partial x} \sin t - \frac{\partial u_y}{\partial y} \cos t \right). \quad (\text{S4})$$

Now the Burgers vector is computed with fixed R by varying the center of the loop (x_0, y_0) throughout the simulation box.

To test the robustness of our findings, we present the spatial distribution of the Burgers vector magnitude $|\vec{b}|$ for three different loop radii R in Fig. S2(a–c). The appearance of the Burgers ring is evident in all cases. To assess the predictive capability of the Eshelby center, we identify the top 1% of the highest $|\vec{b}|$ values and show that their center of mass approximately coincides with the position of the topological defects with winding number -1 in that region, as illustrated in Fig. S2(d–f).

Calculation of D_{\min}^2

To define the local neighborhood (the ‘molecule’), we introduce a sampling radius, chosen as the interaction range r_c . The local strain is determined by minimizing the mean-square difference between the actual displacements of neighboring molecules (relative to a reference molecule) and their expected displacements under a uniform strain ε_{ij} . Specifically, we define

$$D^2(t, \Delta t) = \sum_n \sum_i \left(r_n^i(t) - r_0^i(t) - \sum_j (\delta_{ij} + \varepsilon_{ij}) \times [r_n^j(t - \Delta t) - r_0^j(t - \Delta t)] \right)^2, \quad (\text{S5})$$

where i and j denote spatial coordinates, and n runs over all molecules within the interaction range of the reference molecule ($n = 0$). Here, $r_n^i(t)$ represents the i^{th} component of the position of the n^{th} molecule at time t .

To find the strain tensor ε_{ij} that minimizes D^2 , we compute

$$X_{ij} = \sum_n [r_n^i(t) - r_0^i(t)] \times [r_n^j(t - \Delta t) - r_0^j(t - \Delta t)], \quad (\text{S6})$$

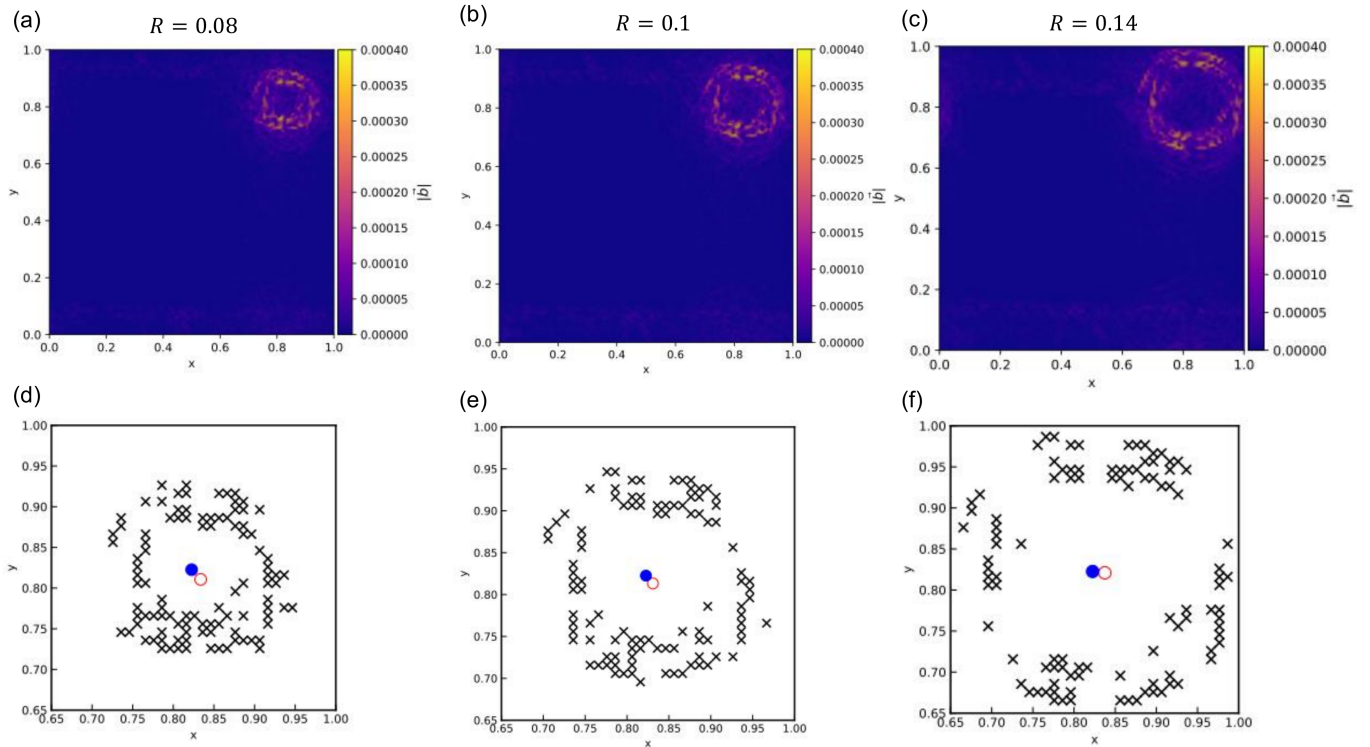


FIG. S2: **(a–c)** Magnitude of the Burgers vector $|\vec{b}|$ computed using three different closed-loop radii, $R = 0.08, 0.01,$ and 0.14 , respectively. The color bar indicates the value of $|\vec{b}|$. **(d–f)** Positions of the top 1% highest $|\vec{b}|$ values are marked with black crosses. The center of mass of these points is indicated by red open circles, while the locations of topological defects with winding number -1 in the corresponding regions are shown as blue filled circles, for the data presented in panels (a), (b), and (c), respectively.

$$Y_{ij} = \sum_n [r_n^i(t - \Delta t) - r_0^i(t - \Delta t)] \times [r_n^j(t - \Delta t) - r_0^j(t - \Delta t)], \quad (\text{S7})$$

$$\varepsilon_{ij} = \sum_k X_{ik} Y_{jk}^{-1} - \delta_{ij}. \quad (\text{S8})$$

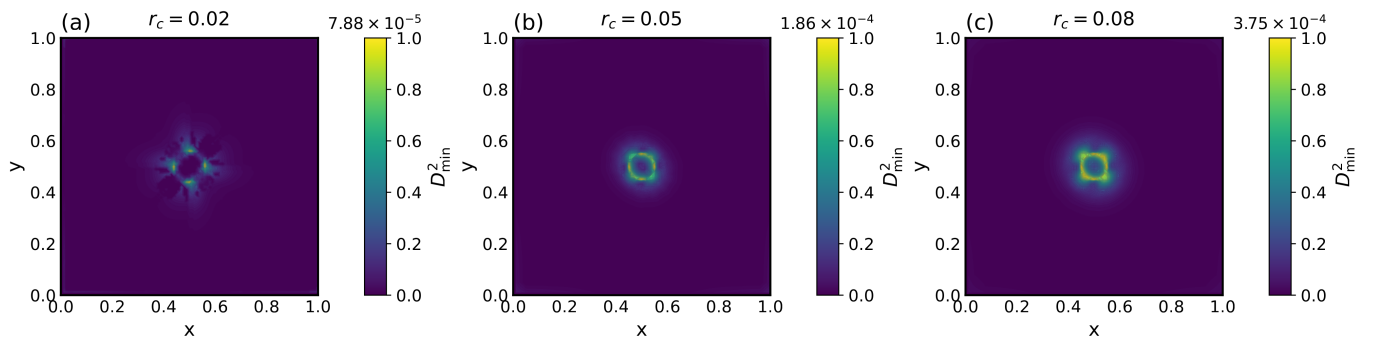


FIG. S3: **(a–c)** The magnitude of D_{min}^2 for an ideal Eshelby inclusion centered at $(x, y) = (0.5, 0.5)$ for different interaction cut-off distance r_c . The parameters for the inclusion have been fixed to $a = 0.05, \varepsilon^* = 1, \nu = 0.46$ and $\phi = \pi/4$.

The minimum value of $D^2(t, \Delta t)$ quantifies the local deviation from the affine deformation over the time interval $[t - \Delta t, t]$, which we refer to as D_{min}^2 .

In order to compute D_{min}^2 for an Eshelby inclusion, we numerically construct a square grid of spacing $l_s = 0.01$ within a unit-length square box. Then we displace each grid point according to the Eqs. (1)-(2), considering them as

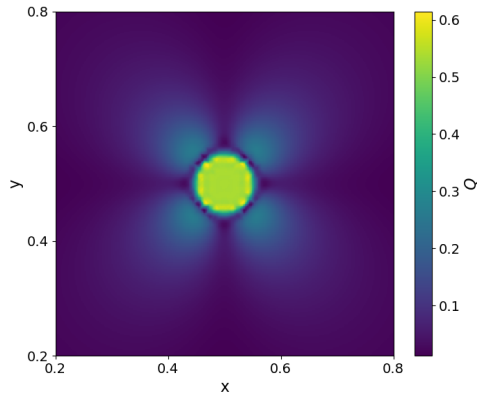


FIG. S4: The magnitude of the quadrupole charge Q , as defined in Eq. (S12), for an ideal Eshelby inclusion centered at $(x_0, y_0) = (0.5, 0.5)$. Parameters are set to $a = 0.05$, $\varepsilon^* = 1$, $\nu = 0.46$ and $\phi = \pi/4$.

point particles. Then we compute D_{\min}^2 for these two consecutive configurations. In Fig. S3 we show the magnitude of D_{\min}^2 for different values of the interaction radius r_c for an ideal Eshelby inclusion centered at $(x, y) = (0.5, 0.5)$. The emergence of circular patterns surrounding the Eshelby center is clearly observable even in D_{\min}^2 values. For the calculation of D_{\min}^2 in the simulation data presented in the main text, we use a cutoff distance of $r_c = 0.05$, which corresponds approximately to the first minimum of the pair correlation function $g(r)$ for the 2D glass sample. However, in simulation data, this quantity does not reflect the symmetric patterns observed in the ideal case, although it effectively captures the approximate regions of plastic deformation.

Analytical solutions for the quadrupole tensor

The quadrupole tensor is derived from the displacement field \vec{u} . The strain tensor is calculated as

$$s_{ij} = \frac{1}{2}(\nabla_i u_j + \nabla_j u_i), \quad (\text{S9})$$

where $i, j = (x, y)$ are Cartesian components. In 2D the components of strain tensor can be computed as

$$s_{xx} = \frac{\partial u_x}{\partial x}, \quad s_{yy} = \frac{\partial u_y}{\partial y}, \quad s_{xy} = s_{yx} = \frac{1}{2} \left(\frac{\partial u_x}{\partial y} + \frac{\partial u_y}{\partial x} \right). \quad (\text{S10})$$

The strain tensor can be decomposed into its trace and traceless parts:

$$\mathbf{s} = m\mathbf{I} + \mathbf{Q}, \quad (\text{S11})$$

where $m = \frac{1}{2}(s_{xx} + s_{yy})$ is the isotropic part, \mathbf{Q} is the traceless deviatoric strain, referred as quadrupole tensor and \mathbf{I} is the identity tensor.

The quadrupole magnitude is

$$Q = \frac{1}{2} \sqrt{(s_{xx} - s_{yy})^2 + 4s_{xy}^2}, \quad (\text{S12})$$

and its orientation is given by

$$\vartheta = \frac{1}{2} \arctan \left(\frac{2s_{xy}}{s_{xx} - s_{yy}} \right). \quad (\text{S13})$$

The normalized deviatoric strain tensor is given by:

$$\mathbf{s}^s = \begin{pmatrix} \cos 2\vartheta & \sin 2\vartheta \\ \sin 2\vartheta & -\cos 2\vartheta \end{pmatrix}, \quad (\text{S14})$$

so that the quadrupole tensor becomes $\mathbf{Q} = Q\mathbf{s}^s$.

We use the analytical expressions for s_{ij} in the case of ideal Eshelby inclusions to plot the quadrupole magnitude Q in Supplementary Fig. S4. The quadrupolar nature of the Eshelby inclusion is evident.